Article:

Ke, C, Shu, S, Zhang, H et al. (2018) On the drag coefficient and averaged Nusselt number of an ellipsoidal particle in a fluid. Powder Technology, 325. pp. 134-144. ISSN: 0032-5910

https://doi.org/10.1016/j.powtec.2017.10.049

On the drag coefficient and averaged Nusselt number of an ellipsoidal particle in a fluid

Chunhai Ke[a], Shi Shu[a], Hao Zhang[b,*], Haizhuan Yuan[a], Dongmin Yang[c]

[a] *Hunan Key Laboratory for Computation and Simulation in Science and Engineering, Xiangtan University, Hunan 411105, P.R. China*
[b] *School of Metallurgy, Northeastern University, Shenyang, Liaoning 110819, P.R. China*
[c] *School of Civil Engineering, University of Leeds, LS2 9JT, UK*

Abstract

The paper aims to improve existing correlations for the drag coefficient and averaged Nusselt number of an ellipsoidal particle in a fluid by additionally considering its orientation. To do so, three dimensional Immersed Boundary - Lattice Boltzmman Method (IB-LBM) simulations were carried out on a classical problem where a hot stationary ellipsoidal particle was passed by continuous cold fluid flows. By changing the shape ($0.25 \leq Ar \leq 2.5$) and incident angle ($0^\circ \leq \theta \leq 90^\circ$) of the solid particle as well as the Reynolds number ($10 \leq Re \leq 200$), the momentum and heat transfer between the solid and fluid phases was quantitatively evaluated and the drag coefficient and averaged Nusselt number were numerically quantified. Then, based on the obtained data, correlations for the drag coefficient and averaged Nusselt number were established by considering Ar, θ and Re as the key influencing factors. Proposed correlations were proven to hold promising prediction capabilities and would be useful to be enclosed in those complex multiphase coupling calculations.

Keywords: Drag coefficient, Averaged Nusselt number, Lattice Boltzmann method, Immersed boundary method, Ellipsoidal particle

---

[*] Corresponding author
Email address: `zhangh@mail.neu.edu.cn` (Hao Zhang)

Preprint submitted to Powder technology *October 30, 2017*

1. Introduction

1.1. Background

Particulate-fluid interaction systems are ubiquitous in various industrial processes whereas present extremely complex momentum and heat transfer characteristics. Available knowledge of these characteristics to date is far from being enough which generates great difficulty in the scaling design and configuration optimization. For the sake of revealing the underlying mechanisms, there are briefly three research hotspots of particular interest at distrinct scales, those are particle scale research, device (macroscopic) scale research and meso-scale research between them [1]. On one hand, all the tuning operations by the engineers are only possible to conduct at the device scale, and then the effect will be eventually imposed on each single particle through complex meso-scale interactions. On the other hand, all the events (*e.g.* turbulence, exchange of momentum and energy, chemical reaction, phase change and deformation of solid particles) taking place at the particle scale form various unpredictably macroscopic phenomenon also via the meso-scale interactions. Therefore, to optimize the operating parameters and energy efficiency, questions remaining open at each level must be answered. In this context, accurate modelling at the particle scale is of paramount importance for preventing irrational predictions.

Recently, Zhong *et al.* [2, 3] have reviewed the state-of-the-art theoretical developments and applications of the combined modelling techniques for particulate-fluid flows. As indicated by the authors [2, 3], the drag coefficient C_d and averaged Nusselt number Nu are the key parameters in the coupled calculations because they are responsible for evaluating the drag force and heat transfer, respectively. Equation 1 gives the typical formula of the drag force and heat flux on a single particle while multi particle systems can be readily considered via an additional term of voidage. In Equation 1, $\mathbf{f}_d$ is the drag force, A is the front area, ρ is the fluid density, u_c is the uniform inlet field velocity far from the particle, q is the heat flux, h_e is the convective heat transfer coefficient of the fluid, S is the surface area, κ is the thermal conductivity coefficient of the fluid, d_p is the volume-equivalent sphere diameter, and T_s and T_f are the temperature of the solid and fluid, respectively. Note that Nu should be obtained prior to the calculation of q since h_e is unknown.

$$\begin{cases} \mathbf{f}_d &= \frac{1}{2} C_d A \rho u_c^2; \\ q &= h_e S(T_s - T_f); \\ Nu &= h_e d_p/\kappa. \end{cases} \tag{1}$$

It is stressed that the drag coefficient and averaged Nusselt number should be evaluated correctly enough by considering many important factors such as the local fluid flow property, particle size/shape/orientation and relative motion/temperature difference between the solid and fluid [4]. To establish accurate correlations for them, several previous studies were carried out aiming to take as many factors as possible into account. However, numerous defects exist in these contributions and hence much further work is still needed. The current study focuses on researching the effect of particle shape and orientation on the drag coefficient and averaged Nu at low Reynolds numbers. The investigation is motivated by the facts that [2, 3]:

- Majority of the solid particles are not regularly spherical in modern industries (over 70%).
- Morphology plays key roles in the particle scale heat and mass transfer characteristics.
- Fundamentals governing above interactions are not well established.

1.2. Previous work

For spherical particles, the correlations of drag coefficients have been well archived and surveyed in the previous literature [4, 5]. However, these correlations for spherical particles have been proven to produce large deviations when applied to non-spherical ones [3]. Hottovy and Sylvester [6] measured the settling velocity of several irregularly shaped particles and found that the drag coefficient for the non-spherical particle is comparable with the spherical one when

$Re < 100$ but significantly higher in the rest testing range of Reynolds number ($100 < Re < 3000$). It is worthwhile noting that sedimentations of irregular particles in fluids (laminar or turbulent, Newtonian or non-Newtonian) were usually used for experimentally determining their drag coefficients [6, 7, 8, 9, 10, 11, 12]. Among these works, Wang *et al.* [11] and Ren *et al.* [12] established the correlations of drag coefficients specially for the cuboid with square base and cylinders, respectively. In the meantime, various shape factors were also defined in different studies, such as the sphericity, particle circularity, Corey shape factor and aspect ratio. These parameters were employed to describe how far the irregular particle deviates from a spherical one and help those general correlations of drag coefficients proposed [13, 14, 9, 10, 15] without specifying the exact particle morphology or orientation.

In addition to the direct experimental measurements, particle-scale numerical simulations have also been carried out for expanding the database of the drag coefficient. Unlike the experimental studies, flow over solid obstacles is the popular cases for the numerical investigations. It is reported by Bokkers *et al.* [16] that, with respect to predict the bubble formation in fluidized beds, using the drag coefficient derived from the lattice Boltzmann method (LBM) simulation [17] produces even better results than using the experiment-based ones [18, 19]. This is not a representative fact showing that experimental can be entirely replaced by numerical simulation. Whereas the comparison results greatly enhance the reliability of the latter technique without doubt. Nowadays, the LBM modelling has been increasingly used to develop the correlations of drag coefficients both for spherical [20, 21, 22, 23, 24, 25, 26, 27] and non-spherical [28, 29, 30] particles. Pioneer studies can be found from Hill *et al.* [20, 21] who proposed a set of drag correlations by considering flow passing through random arrays of spheres in a cubic. Later, Van Der Hoef *et al.* and Beetstra *et al.* investigated flows passing through mono- and bidisperse arrays of spheres at low [22] and moderate [23] Reynolds numbers, respectively. Rong *et al.* carried out similar simulations based on more representative packed structures and proposed novel correlations [24, 25]. Zhou and Fan examined the effect of spherical particle rotation on flows in ordered and random arrays of mono-disperse spheres at low [26] and moderate [27] Reynolds numbers, respectively. As for non-spherical particles, Hölzer and Sommerfeld considered six particle shapes as well as particle rotation in uniform and shear flows and numerically determined the drag, lift and moment coefficients [28]. Rong *et al.* simulated the fluid flow through packed beds of uniform ellipsoids and improved the accuracy of the existing correlations [29]. Guan *et al.* [30] examined the fluid-particle interaction for non-spherical particles at high Reynolds numbers ($0.1 < Re < 3000$) also via the LBM. Besides the LBM simulations, Saha [31] solved three dimensional unsteady Navier Stokes and energy equations to study the wake of a cube placed in a uniform flow. Kishore and Gu [32] used similar numerical methods to examine the momentum transfer phenomena of spheroid particles in an unbounded Newtonian fluid and developed correlations of drag coefficient ($1 < Re < 200$). Richter and Nikrityuk performed numerical simulations and proposed correlations of drag coefficients for cuboidal and ellipsoidal particles [33] with considering angles of attack [34].

Numerical simulations investigating the heat transfer characterstics of non-spherical particles in a fluid were relatively less reported. Wen and Jog numerically studied the effects of Re, particle morphology and other variable properties on the drag coefficient and averaged Nusselt number [35]. Saha examined the transition schemes of flow and thermal field behind a stationary cube by solving the Navier Stokes and energy equations [31]. Kishore and Gu [32] examined the heat transfer phenomena of spheroid particles in an unbounded Newtonian fluid and developed correlations of averaged Nusselt number ($1 < Re < 200, 1 < Pr < 1000$). Then, Reddy and Kishore investigated the effects of wall confinement and the power-law fluid behavior index on momentum and heat transfer phenomena of confined spheroid particles within the same range of Re and Pr [36].

1.3. Motivation and summary of the present work

From the literature survey, it can be seen that the numerical modelling has emerged as a promising method to evaluate drag coefficients and averaged Nusselt number for non-spherical particles. However, available data on the typical morphology is still limited especially for heat transfer though several correlations were proposed before. For example, previous correlations were mainly based on two-dimensional simulation results [32, 35, 36] which need a considerable simplification on the actual particle shape and thus lacked applicability. Richter and Nikrityuk conducted three-dimensional numerical simulations [33, 34] but a systematic study on the difference between oblate and prolate spheroids has not been done. This may be among the reasons why Gan *et al.* [37] adopted the correlation proposed from two-dimensional simulations to investigate the heat transfer in three-dimensional packed and fluidized beds of ellipsoidal particles. Therefore, there is a great need to fill this knowledge gap.

The current paper conducts three-dimensional LBM simulations to investigate the momentum and heat transfer characterstics of ellipsoidal particles in a uniform flow field. By changing the shape ($0.25 \leq Ar \leq 2.5$) and incident angle ($0^\circ \leq \theta \leq 90^\circ$) of the solid particle as well as the Reynolds number ($10 \leq Re \leq 200$), the drag coefficient and averaged Nusselt number under a wide range of conditions are quantified and previous correlations are improved. The rest of the paper is organized as follows. Section 2 briefly gives the mathematics of the LBM and Immersed Boundary Method (IBM) [38]. Section 3 introduces the details of particle generation and calculation platform. In Section 4, validation simulations are carried out. In Section 5, 125 case studies are tested and new correlations for the drag coefficients and averaged Nusselt number are proposed based on the numerical results. At last, some conclusions are drawn in Section 6.

2. Governing equations

2.1. Lattice Boltzmann method

Detailed governing equations and numerical issues can be found in our previous works [39, 40] and thus only the governing equations of LBM are brief introduced here followed by the IBM. In this study, we adopt the D3Q15 model [41] to mimic the heat and mass transfer behaviour of an incompressible Newtonian fluid. The governing equations are the dual distribution models proposed by He *et al.* [42]

$$\begin{cases} f_\alpha(\mathbf{r}+\mathbf{e}_\alpha\delta_t, t+\delta_t) = f_\alpha(\mathbf{r},t) - \frac{f_\alpha(\mathbf{r},t)-f_\alpha^{eq}(\mathbf{r},t)}{\tau_f} + F_\alpha\delta_t \\ g_\alpha(\mathbf{r}+\mathbf{e}_\alpha\delta_t, t+\delta_t) = g_\alpha(\mathbf{r},t) - \frac{g_\alpha(\mathbf{r},t)-g_\alpha^{eq}(\mathbf{r},t)}{\tau_g} + G_\alpha\delta_t \end{cases} \tag{2}$$

where $f_\alpha(\mathbf{r},t)$ and $g_\alpha(\mathbf{r},t)$ represent the fluid density and temperature distribution functions, respectively. In the D3Q15 model, the lattice velocity $\mathbf{e}_\alpha$ reads

$$\mathbf{e}_\alpha = \begin{cases} (0,0,0) & \alpha = 0 \\ (\pm c,0,0),\ (0,\pm c,0),\ (0,0,\pm c) & \alpha = 1,2,3,4,5,6 \\ (\pm c,\pm c,\pm c). & \alpha = 7,8,9,10,11,12,13,14 \end{cases} \tag{3}$$

where c is the lattice speed. The superscript eq in Equation 2 means equilibrium

$$\begin{cases} f_\alpha^{eq}(\mathbf{r},t) = \rho\omega_\alpha[1+3(\mathbf{e}_\alpha\cdot\mathbf{u}) + \frac{9}{2}(\mathbf{e}_\alpha\cdot\mathbf{u})^2 - \frac{3}{2}\mid\mathbf{u}\mid^2] \\ g_\alpha^{eq}(\mathbf{r},t) = T\omega_\alpha[1+3(\mathbf{e}_\alpha\cdot\mathbf{u}) + \frac{9}{2}(\mathbf{e}_\alpha\cdot\mathbf{u})^2 - \frac{3}{2}\mid\mathbf{u}\mid^2] \end{cases} \tag{4}$$

where $\mathbf{r}$ is the space position vector, $\mathbf{e}_\alpha$ is the fluid velocity, δ_t is the discrete time step. The values of the weights are: $\omega_0 = 2/9$, $\omega_\alpha = 1/9$ for $\alpha = 1-6$ and $\omega_\alpha = 1/72$ for $\alpha = 7-14$, $\mathbf{u}$ denotes the macro fluid velocity at each lattice node which can be calculated by $\mathbf{u} = (\sum_{\alpha=0}^{14} f_\alpha e_\alpha + \frac{1}{2}F_B\delta_t)/\rho_f$, the macro fluid density is $\rho = \sum_{\alpha=0}^{14} f_\alpha$ and the macro temperature can be calculated by $T = \sum_{\alpha=0}^{14} g_\alpha e_\alpha + \frac{1}{2}Q_B\delta_t$. t denotes time, τ_f and τ_g denote the non-dimensional relaxation times of the density and temperature evolutions, respectively, which can be expressed as

$$\begin{cases} \tau_f = \dfrac{L_c u_c}{Re c_s^2 \delta_t} + 0.5 \\ \tau_g = \dfrac{L_c u_c}{Re Pr c_s^2 \delta_t} + 0.5 \end{cases} \tag{5}$$

where c_s is the lattice speed of sound, L_c and u_c are the characteristic length and velocity, respectively. $Re = \rho u_c L_c / \mu$ and $Pr = c_p \mu / \kappa$ are the Reynolds and Prandtl numbers, respectively. c_p and μ are the specific heat capacity and kinetic viscosity, respectively. F_α and G_α in Equation 2 are the source terms which are evaluated via the IBM in Section 2.2.

2.2. Immersed boundary method

In this study, the momentum exchange-based IBM proposed by Niu *et al.* [43] is adopted to treat the boundary conditions on the particle surface. Firstly, we introduce an important tool, the discrete Delta function [38]

$$D_{ijk}(\mathbf{r}_{ijk} - \mathbf{X}_l) = \frac{1}{h^3} \delta_h \left(\frac{x_{ijk} - X}{h} \right) \delta_h \left(\frac{y_{ijk} - Y}{h} \right) \delta_h \left(\frac{z_{ijk} - Z}{h} \right) \tag{6}$$

where $\mathbf{X}_l(X, Y, Z)$ is the solid coordinate, the subscript l denotes those variables at the location of the solid particles, $\sum\limits_l$ stands for a loop on all the Lagrangian points on the particle surface, h is the LBM mesh spacing and

$$\delta_h(a) = \begin{cases} \frac{1}{4}(1 + cos(\frac{\pi |a|}{2})), & when \mid a \mid \leq 2 \\ 0, & otherwise \end{cases} \tag{7}$$

Using Equations 6 and 7, the fluid macro variables at the solid locations can be numerically obtained. Meanwhile, the effect of solid movement and temperature difference on the fluid flow can also be possibly considered. For example, the fluid velocity and temperature on the solid particles are evaluated using the

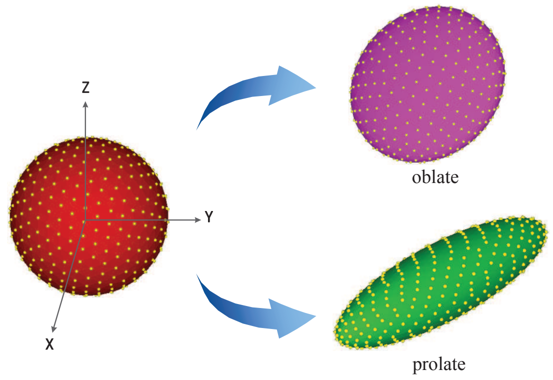

Figure 1: Typical spheroidal particles: sphere, prolate spheroid and oblate spheroid.

numerical interpolation from the circumambient fluid points as below

$$\begin{cases} \mathbf{u_f}(\mathbf{X}_l,t) = \sum\limits_{ijk} \mathbf{u_f}(\mathbf{r},t) D_{ijk}(\mathbf{r}_{ijk} - \mathbf{X}_l) h^3 \\ T_f(\mathbf{X}_l,t) = \sum\limits_{ijk} T_f(\mathbf{r},t) D_{ijk}(\mathbf{r}_{ijk} - \mathbf{X}_l) h^3 \end{cases} \tag{8}$$

Then, these velocity and temperature distribution functions are modified by the local particle velocity and heat transfer between the two phases with different temperatures, respectively. Based on the momentum exchange rule, the source terms F_α and G_α in Equation 2 can be calculated now as

$$\begin{cases} F_\alpha = \left(1 - \frac{1}{2\tau_f}\right) \omega_\alpha \left(3\frac{\mathbf{e}_\alpha - \mathbf{u}}{c^2} + 9\frac{\mathbf{e}_\alpha \cdot \mathbf{u}}{c^4} e_\alpha\right) \cdot \mathbf{F}_B(\mathbf{r},t), & for\ velocity\ BC \\ where, \mathbf{F}_B(\mathbf{r},t) = \sum\limits_l \mathbf{F}_f(\mathbf{X}_l,t) D_{ijk}(\mathbf{r}_{ijk} - \mathbf{X}_l) \Delta s_l, & \\ where, \mathbf{F}_f(\mathbf{X}_l,t) = 2\rho(\mathbf{X}_l,t)(\mathbf{u}_s(\mathbf{X}_l,t) - \mathbf{u}_f(\mathbf{X}_l,t)) h/\delta t, & \\ G_\alpha = \left(1 - \frac{1}{2\tau_g}\right) \omega_\alpha Q_B(\mathbf{r},t), & for\ thermal\ BC \\ where, Q_B(\mathbf{r},t) = \sum\limits_l Q(\mathbf{X}_l,t) D_{ijk}(\mathbf{r}_{ijk} - \mathbf{X}_l) \Delta s_l, & \\ where, Q(\mathbf{X}_l,t) = 2(T_s(\mathbf{X}_l,t) - T_f(\mathbf{X}_l,t)) h/\delta_t. & \end{cases} \tag{9}$$

where Δs_l is the area that each Lagrangian point occupies on the particle sur-

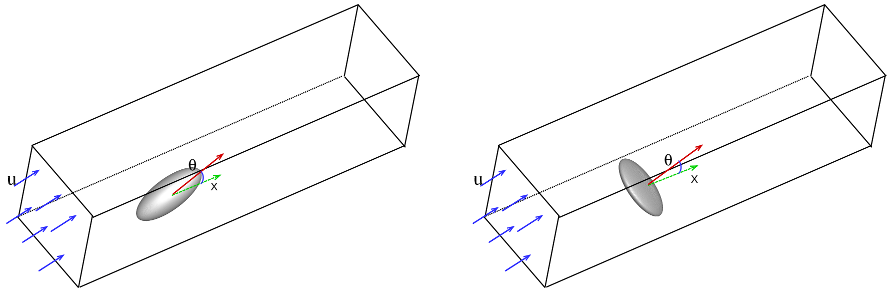

(a) (b)

Figure 2: Characteristics of ellipsoidal particles and the incident angle θ: (a) Prolate spheroid; (b) Oblate spheroid.

face. The averaged Nusselt number is calculated as [44]

$$Nu = \frac{\sum_l Q(\mathbf{X}_l, t)\Delta s_l}{\kappa S(T_h - T_c)} d_p \tag{10}$$

where T_h and T_c denote the high and low temperature in the system, respectively.

3. Computational approaches

3.1. Mesh generation

In this paper, we consider two types of ellipsoidal particles, namely the prolate and oblate spheroids, which can be well defined in Cartesian coordinates by

$$\frac{x^2}{\breve{a}^2} + \frac{y^2}{\breve{b}^2} + \frac{z^2}{\breve{c}^2} = 1. \tag{11}$$

where the parameters $\breve{a}$, $\breve{b}$ and $\breve{c}$ in Equation 11 are the principal semi-axes along X direction, Y direction and Z direction, respectively. It is noted that in this paper we only consider the spheroids with two equal axes, $\breve{b} = \breve{c}$, and

Table 1: Specifications of our test platform

Operating System	CentOS 7.3
CPU Type	Intel(R) Xeon(R) CPU E5-2620 v4
CPU Clock	2.10GHz × 32 cores
Host Memory Size	96GB
GPU Type	NVIDIA Tesla K40C
GPU Clock	3.0 GHz × 2880 cores
Device Memory Size	12.0 GB
Host Compiler	g++ (GCC) 4.8.5
Device Compiler	nvcc 8.0

thus the aspect ratio is defined as $Ar = \check{a}/\check{b}$ or $Ar = \check{a}/\check{c}$. In such a case, it stands for a sphere when $Ar = 1$, a prolate spheroid when $Ar > 1$ and an oblate spheroid when $Ar < 1$ as shown in Figure 1.

During the IB-LBM calculation, the solid particle should be further constructed by Lagrangian points. In this paper, mesh generation on particle surface is performed based on the software package following two steps. Firstly, the CVDT grids are formed on the surface of a unit sphere with approximately equal size. Then, the Lagrangian points on the surface of a spherical particle are mapped into an ellipsoid by topological transformation as shown in Figure 1. The advantage of this treatment is that the unit sphere grid can be called many times for generating multiple particles with different sizes, spatial distributions and velocities. The orientation of the ellipsoidal particle is also considered as a key factor in this study. For the sake of clarification, the incident angle θ for the two cases are indicatively shown in Figure 2.

3.2. CUDA introduction and parameters of platforms

For three dimensional IB-LBM simulations, the grid number is very large and the efficiency of computations on CPUs is relatively low. In this paper, the in-house code is implemented based on the CPU-GPU heterogeneous architecture [45]. In the CPU-GPU heterogeneous computer system, the GPU cooperates with the CPU in the complicated calculation progress. One of the

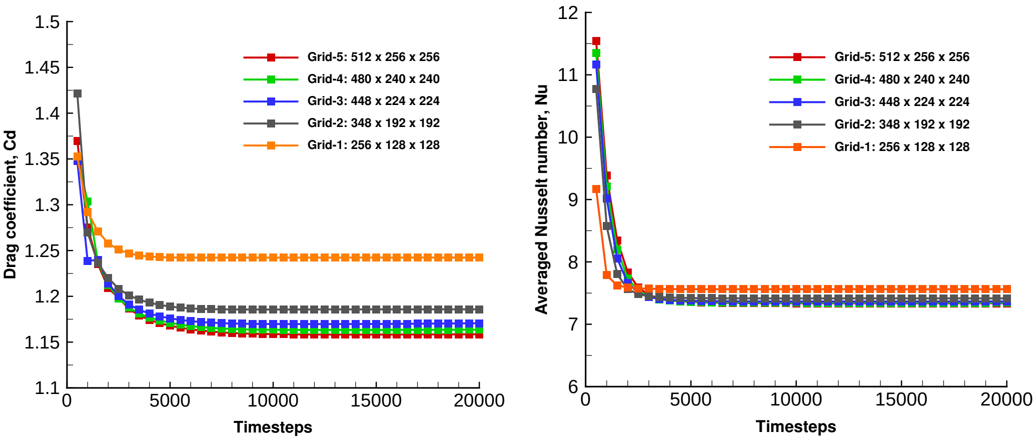

(a) (b)

Figure 3: Flow past a sphere at Re=100 ((a) Temporal variations drag coefficient, (b) Temporal variations averaged Nusselt number) .

main drawbacks of using such an architecture for applications is that it is necessary to exchange data between the CPU host and the GPU device frequently. Data must be moved to the GPU memory, and parallel kernels are launched asynchronously on the GPU by the host. To avoid this, in the current study, the main calculations are run on the GPU, and data exchange function is called only when output data is needed. Table 1 lists the specifications of our platform.

4. Validation case

Though the in-house IB-LBM code has been validated in several previous studies [46, 47], there is a need to further validate its capability on the current application. In this paper, we consider a three dimensional duct containing a hot stationary ellipsoidal particle which is passed by continuous cold fluid flows as shown in Figure 2. The solid particle plays a role as an obstacle to interrupt the flow field meanwhile a heat source to heat the surrounding fluid. We firstly carry out the validation on a sphere in Section 4.1, then further on a spheroid in Section 4.2. In all the simulations of this paper, the characteristic velocity

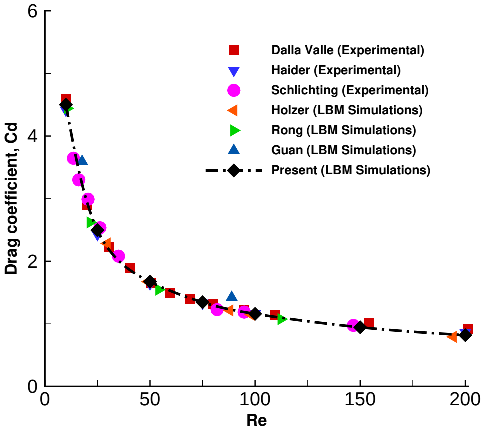

Figure 4: Comparison of drag coefficients for the flow around a sphere at different Reynolds numbers.

$u_c = 0.05$ and the velocities of the four solid boundary are also set as 0.05. The temperature is normalized by $\tilde{T}_f = (T_f - T_c)/(T_h - T_c)$ in the non-dimensional calculations. So $\tilde{T}_s = 1$ and $\tilde{T}_f = 0$ are set on the solid and in the entire initial flow field, respectively. The characteristic length is the volume-equivalent sphere diameter, $L_c = d_p$ and $Pr = 0.744$.

In order to increase the computational efficiency, we decide to pick a relatively small computational domain '$20d_p \times 10d_p \times 10d_p$' following the work of Gilmanov *et al.* [48], Zastawny *et al.* [49], Rong *et al.* [24] and Guan *et al.* [30]. The grid independence test on the spherical case suggests that a large number of grids are needed to obtain accurate results. By considering the grid effect on both C_d and averaged Nu as shown in Figure 3, we decide to adopt 'Grid-5' to conduct all the simulations which hold nearly $34M$ grid points.

4.1. Spherical case

For this classic case, flow passing a sphere has been carried out by a large number of studies both through numerical simulations and experiments, and several semi-empirical formula of drag coefficient C_d and averaged Nu are available. In Figure 4, numerical results of the drag coefficients from the current study are listed which are in line with those taken from the references (Haider

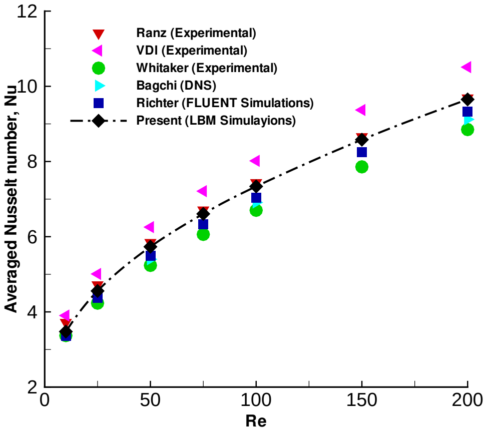

Figure 5: Comparison of averaged Nusselt numbers for the flow around a sphere at different Reynolds numbers.

and Levenspiel [50], DallaValle [51], Schlichting and Gersten [52], Hölzer and Sommerfeld [53], Rong *et al.* [24] and Guan *et al.* [30]). It is clearly shown that the drag coefficient C_d decreases rapidly with the increase of Re. Here we particularly tabulated several numerical results also from LBM simulations using comparable calculation domains and mesh systems [53, 24, 30] and good agreements are reached.

Similar comparisons are performed on the obtained averaged Nusselt number as shown in Figure 5 together with the data from Richter and Nikrityuk [54], Bagchi *et al.* [55], Ranz [56], VDI [57] and Whitaker [58]. Different to the drag coefficient C_d, it is found that the averaged Nusselt number increases with Re and larger discrepancies are found among the data sources which also increase with Re. The currently reported results are higher than the numerical results obtained by other methods but still hold the accordance with the reference at an acceptable level.

4.2. Ellipsoidal case

Following the study of spherical particles in the above subsection, here we test the sensitivity of drag coefficients to the particle morphology Ar, the incident angle θ and Re. We consider the cases with two kinds of Ar (0.5 and

2.5) and three kinds of θ (0°, 45° and 90°) at different Re ($10 \sim 300$) for the validation purpose. Figure 6 shows the drag coefficients for the flow around ellipsoidal particles at different Reynolds numbers and incident angles θ. It can be seen that, similar with the spherical case, the drag coefficient for non-spherical particles also decreases when Re increases, regardless of θ. Moreover, the high sensitivity of the drag coefficient for non-spherical particles to the changes of θ is expected. For the oblate spheroids as shown in Figure 6a, at a given Re, the drag coefficient decreases with the increase of the incident angle but the opposite is true for the prolate ones in Figure 6b. This is because the front area of the oblate spheroid is the largest when $\theta = 0°$ which gradually decreases when further increasing θ. As for the prolate one, the front area is the largest when this long body stands up, so the blocking effect is strongly enhanced when $\theta = 90°$. Our numerical results show good agreements with those of Rong *et al.* [29] also based on LBM simulations. The predicted drag coefficients by Haider *et al.* [50] based on the experimental data are also attached in the figure for comparison. It is important to point out that Haider *et al.* [50] used the sphericity ϕ to describe the particle shape which is a coarse approximation of the exact particle morphology (prolate or oblate) and thus considering the incident angle is not possible in the model.

Through two steps of validations, the capability of the current model is demonstrated. Influence of different factors on the drag coefficient and averaged Nusselt number will be discussed in detail in the following sections.

5. Results and discussions

By changing the shape (Ar changes from 0.25, 0.5, 1.0, 2.0 to 2.5) and incident angle (θ changes from 0°, 30°, 45°, 60° to 90°) of the solid particle as well as the Reynolds number (Re changes from 10, 20, 50, 100 to 200), 125 cases in total are numerically studied. For the currently considered simulations, the fluid temperature distribution is briefly determined by the flow field. However, the flow field is hardly influenced by the temperature difference. Therefore, the

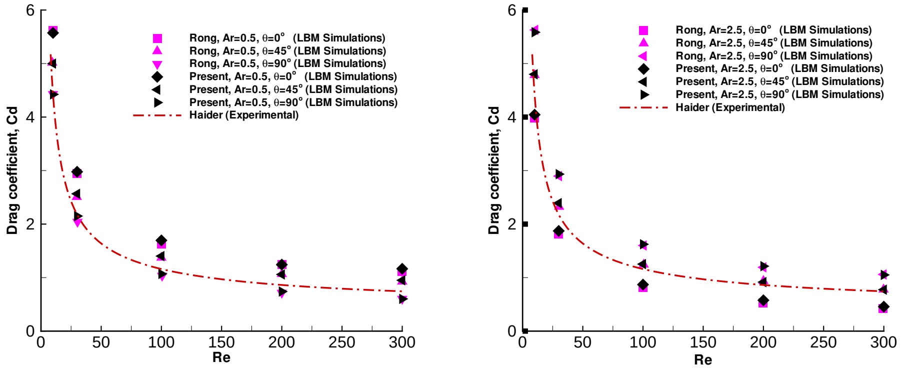

(a) (b)

Figure 6: Comparison of drag coefficients for the flow around ellipsoidal particles at different Reynolds numbers and incident angles θ (a) oblate: Ar=0.5 and (b) prolate: Ar=2.5.

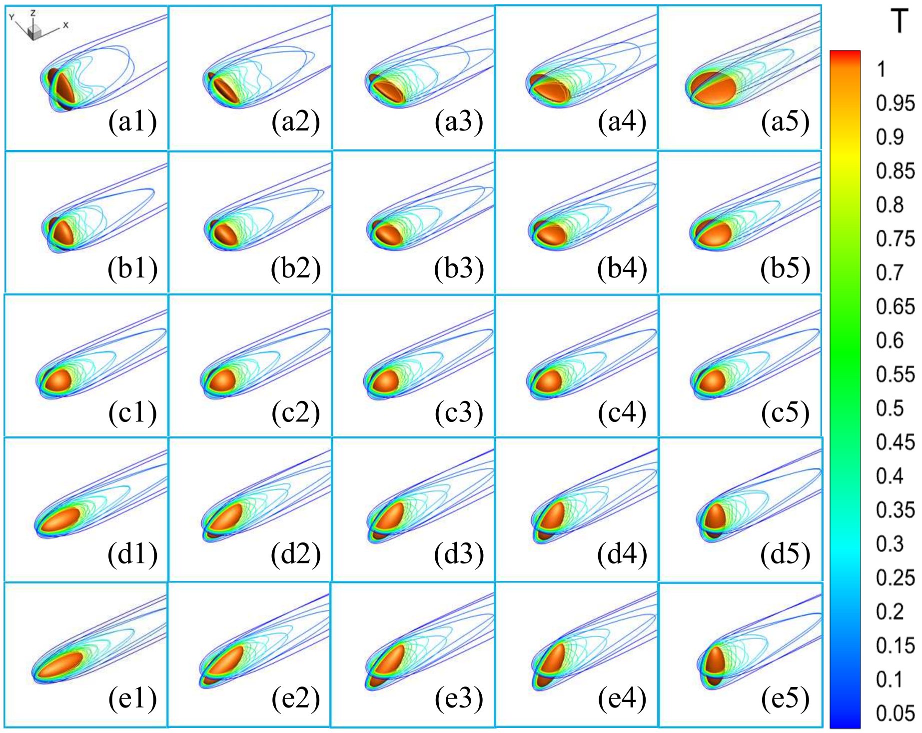

Figure 7: Temperature distributions at $Re = 50$ in different cases. From a to e, Ar changes from 0.25, 0.5, 1.0, 2.0 to 2.5. From 1 to 5, θ changes from 0°, 30°, 45°, 60° to 90°.

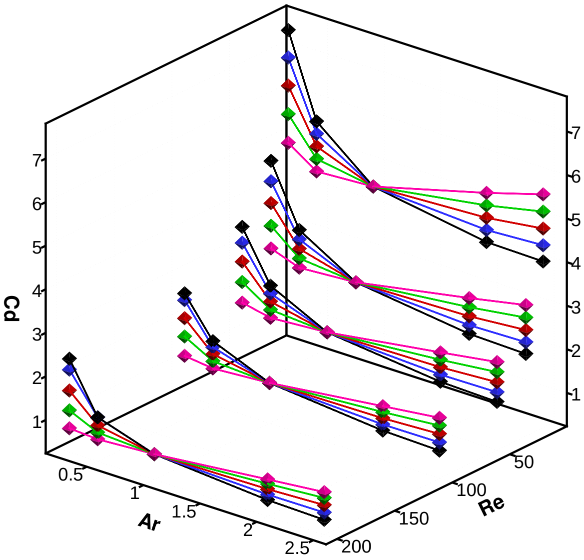

Figure 8: Drag coefficients at different Re, Ar and θ (Black: $\theta = 0°$, Blue: $\theta = 30°$, Red: $\theta = 45°$, Green: $\theta = 60°$, Magenta: $\theta = 90°$).

temperature distribution is a good indication for the overall performance of the whole system. Figure 7 shows the temperature distributions at $Re = 50$ as a typical case of all the considered ones where combined influence of Ar and θ on the local temperature can be observed. By comparing Figure 7 a1, b1, c1, d1 and e1 (Ar changes from 0.25, 0.5, 1.0, 2.0 to 2.5, $\theta = 0°$ and $Re = 50$), it can be seen that the temperature contour behind the particle changes gradually from a bow-shaped profile to an elliptic one with the increase of Ar. The same trend can be also observed when comparing Figure 7 a1, a2, a3, a4 and a5 (θ changes from 0°, 30°, 45°, 60° to 90°, $Ar = 0.25$ and $Re = 50$). Therefore, it is fair to conclude that the bow-shaped profile is highly influenced by the front area. At a given Re, the bow-shaped profile intends to appear when the front area is large enough. It is worthwhile mentioning that the flow fields behind the particles show unsteady regimes when ($Re = 200$, $Ar = 0.25$, $\theta = 0°$) and ($Re = 200$, $Ar = 0.25$, $\theta = 30°$) which are not found in other cases. Time-averaged values are used in these two unsteady cases. These transition phenomenons were also discussed in the work of Richter and Nikrityuk [33].

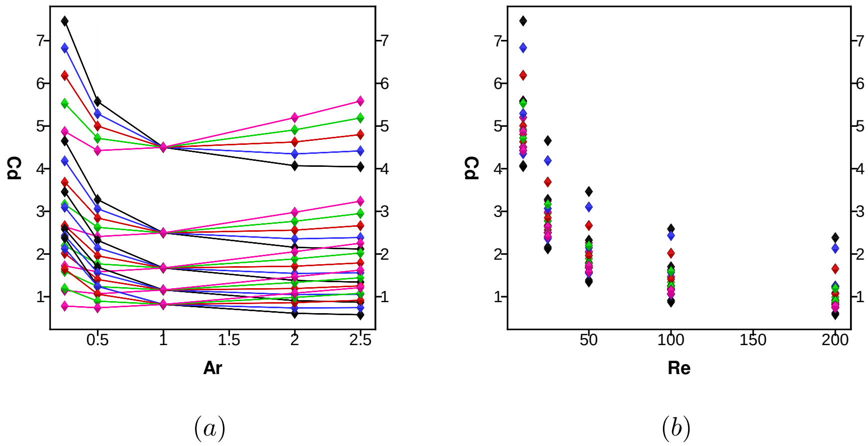

(*a*) (*b*)

Figure 9: (a) Projection of drag coefficients on Y-Z coordinate plane (b) Projection of drag coefficients on X-Z coordinate plane (Black: $\theta = 0°$, Blue: $\theta = 30°$, Red: $\theta = 45°$, Green: $\theta = 60°$, Magenta: $\theta = 90°$).

5.1. Drag coefficient

Figure 8 shows the drag coefficients at different Re, Ar and θ, quantitatively. It can be seen that C_d is significantly influenced by Re, Ar and θ. For a given particle shape and orientation, C_d is reduced sharply when increasing Re. This trend can be clearly seen in the 2D drawing in Figure 9b. For a given Re, Ar and θ present a mixed influence on C_d which is due to the front area as mentioned in the above section. For example in Figures 8 and 9a, C_d of the prolate spheroid ($Ar > 1$) increases with θ and the opposite relation is found for the oblate spheroid ($Ar < 1$). The trend is more obvious at large $|Ar - 1|$ and also explains the fact why the five lines in Figures 8 and 9a cross at $Ar = 1$ for a given Re.

As mentioned above, there have been quite a number of available correlations both on the drag coefficient and the averaged Nusselt number. Apart from the limited working conditions, the formula of these correlations hold quite different forms. From the practicality point of view, it is necessary to make a balance between their accuracy and complexity. In other words, the simpler forms with acceptable accuracy are more welcome. Through a survey of references, it is

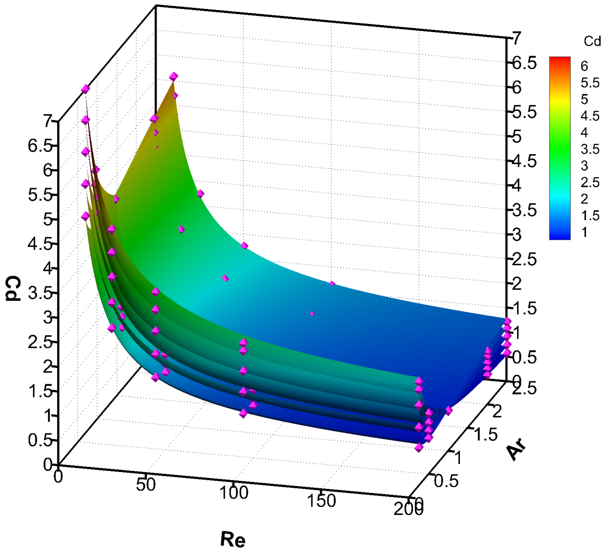

Figure 10: Predicted C_d by the proposed correlation with numerical results.

decided to construct the new correlation for the drag coefficient based on the forms suggested by [59, 33, 34]

$$C_d = \frac{\Lambda_1}{Re} + \frac{\Lambda_2}{\sqrt{Re}} + \Lambda_3. \quad (12)$$

Particularly, the effect of the incident angle, $\zeta = \theta\pi/180°$, should be easily peeled off and added in for those specified applications. Therefore, the new formula for the drag coefficient is given as

$$C_d = \frac{c_1}{Re}(Ar)^{c_2} + \frac{c_3}{\sqrt{Re}}(Ar)^{c_4} + c_5(Ar)^{c_6} + (Ar)^{c_7}(Ar-1)\frac{c_8}{Re^{c_9}} sin^2(c_{10}\zeta). \quad (13)$$

Through a regression analysis on the data in Figure 8, the unknown coefficients in Equation 13 are determined as

$$c_1 = 18.7371; c_2 = 0.2883; c_3 = 7.9738; c_4 = -0.5126; c_5 = 0.1938;$$

$$c_6 = -1.1848; c_7 = -0.5531; c_8 = 2.6334; c_9 = 0.2199; c_{10} = 0.9865.$$

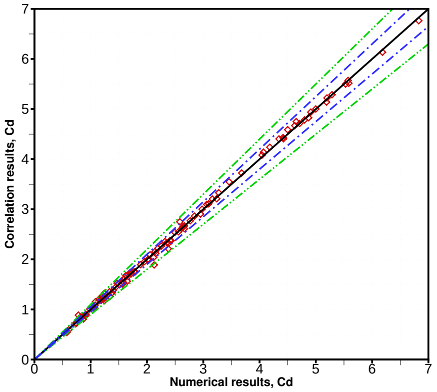

Figure 11: Comparison between the present numerical and correlated drag coefficients. Dash-dot lines stand for the relative error of ±5% and ±10%.

Note that in Equation 13, the last term on the right hand side stands for the effect of the incident angle and it vanishes when $Ar = 1$ or $\zeta = 0$. Figure 10 shows the predicted C_d by the proposed correlation compared with numerical results. It can be seen that the proposed correlation can produce quite similar distributions on the drag coefficients in a wide range of working conditions. Quantitative comparisons can be found in Figure 11, and the averaged relative deviation is $\bar{\varepsilon}_{C_d} = 2.1\%$.

5.2. Averaged Nusselt number

Figure 12 shows the averaged Nusselt number at different Re, Ar and θ. Similar with C_d, the influences of Re, Ar and θ on Nu are also multiple. For a given particle shape and orientation, Nu increases along with Re (also can see from the 2D drawing in Figure 13 b). From Figure 12 and Figure 13 a, it can be seen that the effect of θ on the prolate spheroid ($Ar > 1$) is larger than the oblate one ($Ar < 1$). For the prolate spheroid at a given Re and Ar, Nu increases with θ which is in line with Richter and Nikrityuk [33]. Moreover, at a given Re, Nu increases with Ar when $\theta > 45°$, decreases with the increase of Ar when $\theta < 45°$ and does not change much with Ar when θ approaches to

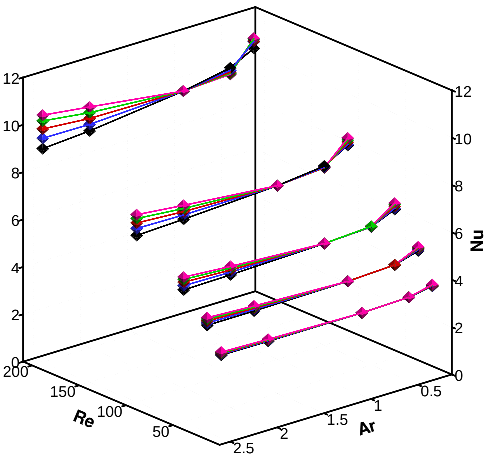

Figure 12: Averaged Nusselt numbers at different Re, Ar and θ (Black: $\theta = 0°$, Blue: $\theta = 30°$, Red: $\theta = 45°$, Green: $\theta = 60°$, Magenta: $\theta = 90°$).

45°. This influence trend of θ is enhanced when increasing Re. However, for the oblate spheroid, Nu declines with the increase of Ar for all the considered incident angles. It is observed from the numerical results that at a given Re and Ar, Nu for the oblate spheroid decreases with the increase of θ when $Ar = 0.5$ but increases with θ when $Ar = 0.25$.

We also consider a simple formula for the averaged Nusselt number [58]

$$Nu = \Lambda_1 Pr^{1/3} Re^{2/3} + \Lambda_2 Pr^{1/3} Re^{1/2} + \Lambda_3. \tag{14}$$

The new formula for the averaged Nusselt number is given as

$$Nu = c_1 Pr^{1/3} Re^{2/3} (Ar)^{c_2} + c_3 Pr^{1/3} Re^{1/2} (Ar)^{c_4} + c_5 (Ar)^{c_6} + (Ar)^{c_7} (Ar-1) c_8 Re^{c_9} sin^2(c_{10}\zeta). \tag{15}$$

where

$$c_1 = 0.0187; c_2 = 0.8829; c_3 = 0.5453; c_4 = -0.1830; c_5 = 1.9120;$$

$$c_6 = 0.0646; c_7 = 0.7346; c_8 = 0.0227; c_9 = 0.5660; c_{10} = 1.0645.$$

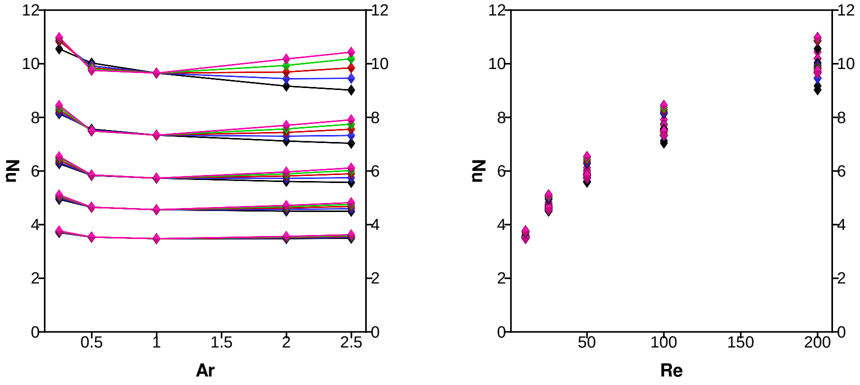

(a) (b)

Figure 13: (a) Projection of averaged Nusselt numbers on Y-Z coordinate plane (b) Projection of averaged Nusselt numbers on X-Z coordinate plane (Black: $\theta = 0°$, Blue: $\theta = 30°$, Red: $\theta = 45°$, Green: $\theta = 60°$, Magenta: $\theta = 90°$).

Figure 14 shows the predicted Nu by Equation 15 compared with numerical results and the averaged relative deviation is $\bar{\varepsilon}_{Nu} = 1.4\%$ as shown in Figure 15.

6. Concluding remarks

Three dimensional IB-LBM simulations were carried out on a classic problem where a hot stationary ellipsoidal particle is passed by continuous cold fluid flows. By changing the shape and orientation of the solid particle as well as the Reynolds number, the momentum and heat transfer between the solid and fluid phases are quantitatively evaluated and the drag coefficient and averaged Nusselt number are numerically quantified under a wide range of working conditions ($0.25 \leq Ar \leq 2.5$, $0° \leq \theta \leq 90°$, $10 \leq Re \leq 200$ and $Pr = 0.744$).

It is found that both the drag coefficient and averaged Nusselt number of an ellipsoidal particle are influenced by the shape, incident angle and Reynolds number. For a given particle shape and orientation, Nu increases but C_d decreases with elevated Re. For a given Re, C_d of the prolate spheroid increases with θ and the opposite relation is found for the oblate spheroid. This trend

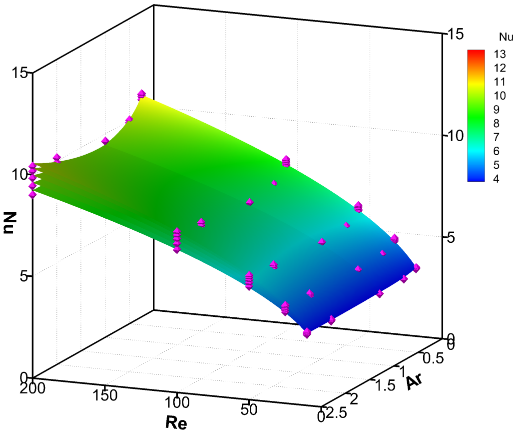

Figure 14: Predicted Nu by the proposed correlation with numerical results.

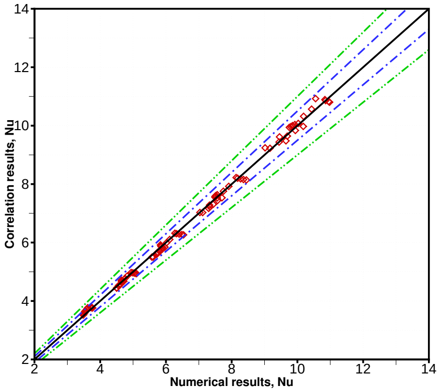

Figure 15: Comparison between the present numerical and correlated Nusselt number. Dash-dot lines stand for the relative error of ±5% and ±10%.

becomes more obvious at large $|Ar-1|$. The effect of θ on the averaged Nusselt number of the prolate spheroid is higher than the oblate one. For the prolate spheroid at a given Re and Ar, Nu increases with θ. At a given Re, Nu increases with Ar when $\theta > 45°$, decreases with the increase of Ar when $\theta < 45°$ and does not change much with Ar when θ approaches to $45°$. This influence trend of θ is enhanced when increasing Re. For the oblate spheroid, Nu declines with the increase of Ar for all the considered incident angles.

At last, based on the numerical results, correlations for the drag coefficient and averaged Nusselt number are established by considering Ar, θ and Re as the key influencing factors. The correlations hold very good accuracy, easy forms and thus are convenient to be used in the macro scale modelling such as in the Eulerian-Lagrangian coupling framework.

Conflict of interest

The authors declared that they have no conflicts of interest to this work.

Acknowledgments

This work is financially supported by the National Science Foundation of China (11571293, 51606040, 11501484, 11601462), Jiangsu Province Science Foundation for Youths (BK20160677), and Hunan Provincial Innovation Foundation for Postgraduate (CX2016B246).

Nomenclature

α	LBM index (subscript)
$\breve{a}$	Principal semi-axes of ellipsoid along X direction
$\check{b}$	Principal semi-axes of ellipsoid along Y direction
$\check{c}$	Principal semi-axes of ellipsoid along Z direction
Δs_l	Area that each Lagrangian point occupies on the particle surface

$\delta(\cdot)$	Delta function
δ_t	Fluid discrete time step
κ	Thermal conductivity coefficient
$\Lambda_1, \Lambda_2, \Lambda_3$	Coefficient of fitting formula
$\mathbf{e}_\alpha$	Fluid velocity
$\mathbf{r}$	Fluid space position vector
$\mathbf{u_f}$	Local fluid velocity
$\mathbf{u_s}$	Local particle velocity
$\mathbf{u}$	Fluid macro velocity
$\mathbf{X}_l$	Solid coordinate
μ	Fluid kinetic viscosity
ω	Fluid value of weight
$\overline{\varepsilon}_{C_d}$	Averaged relative deviation of drag coefficient
$\overline{\varepsilon}_{Nu}$	Averaged relative deviation of averaged Nusselt number
ρ	Fluid macro density
τ_f	Fluid non-dimensional relaxation time of the density evolution
τ_g	Fluid non-dimensional relaxation time of the temperature evolution
$\mathbf{f}_d$	Drag force
θ	Incident angle
$\tilde{T}_f$	Normalized fluid temperature
$\tilde{T}_s$	Normalized solid temperature
$\varepsilon_{_{Nu}}$	Relative errors for averaged Nusselt number

ε_{C_d}	Relative errors for drag coefficient
A	Front area
Ar	Aspect ratio
c	Fluid lattice speed
C_d	Drag coefficient
c_p	Specific heat capacity
c_s	Fluid lattice speed of sound
d_p	Volume-equivalent sphere diameter
F_α	External force
f_α	Fluid density distribution function
f_α^{eq}	Fluid equilibrium density distribution function
G_α	External heat source
g_α	Fluid temperature distribution function
g_α^{eq}	Fluid equilibrium temperature distribution function
h	Fluid mesh spacing
h_e	Convective heat transfer coefficient of the fluid
L_c	Characteristic length
Nu	Averaged Nusselt number
Pr	Prandtl number
q	Heat flux
Re	Reynolds number
S	Total area of the particle surface

T	Fluid macro temperature
T_c	Low temperature
T_f	Local fluid temperature
T_h	High temperature
T_s	Local particle temperature
u_c	Characteristic velocity

References

[1] H. Zhu, Z. Zhou, Q. Hou, A. Yu, Linking discrete particle simulation to continuum process modelling for granular matter: Theory and application, Particuology 9 (4) (2011) 342–357.

[2] W. Zhong, A. Yu, G. Zhou, J. Xie, H. Zhang, CFD simulation of dense particulate reaction system: Approaches, recent advances and applications, Chemical Engineering Science 140 (2016) 16–43.

[3] W. Zhong, A. Yu, X. Liu, Z. Tong, H. Zhang, DEM/CFD-DEM modelling of non-spherical particulate systems: Theoretical Developments and Applications, Powder Technology 302 (2016) 108–152.

[4] R. Clift, J. Grace, T. Weber, Bubbles, drops and particles, Academic Press, 1978.

[5] A. Khan, J. Richardson, Fluid-particle interactions and flow characteristics of fluidized beds and settling suspensions of spherical particles, Chemical Engineering Communications 78 (1) (1989) 111–130.

[6] J. D. Hottovy, N. D. Sylvester, Drag coefficients for irregularly shaped particles, Ind. Eng. Chem. Process Des. Dev 18 (3) (1979) 433–436.

[7] G. Kasper, T. Niida, M. Yang, Measurements of viscous drag on cylinders and chains of spheres with aspect ratios between 2 and 50, Journal of Aerosol Science 16 (6) (1985) 535–556.

[8] K. Renganathan, R. Turton, N. N. Clark, Accelerating motion of geometric and spherical particles in a fluid, Powder Technology 58 (4) (1989) 279–284.

[9] S. F. Chien, Settling velocity of irregularly shaped particles, Society of Petroleum Engineers 9:4 (4) (1994) 281–289.

[10] S. Tran-Cong, M. Gay, E. E. Michaelides, Drag coefficients of irregularly shaped particles , Powder Technology 139 (1) (2004) 21 – 32.

[11] J. Wang, H. Qi, J. Zhu, Experimental study of settling and drag on cuboids with square base , Particuology 9 (3) (2011) 298 – 305.

[12] B. Ren, W. Zhong, B. Jin, Y. Lu, X. Chen, R. Xiao, Study on the drag of a cylinder-shaped particle in steady upward gas flow, Industrial & Engineering Chemistry Research 50 (12) (2011) 7593–7600.

[13] A. Haider, O. Levenspiel, Drag coefficient and terminal velocity of spherical and nonspherical particles, Powder Technology 58 (1) (1989) 63 – 70.

[14] G. H. Ganser, A rational approach to drag prediction of spherical and nonspherical particles, Powder Technology 77 (2) (1993) 143 – 152.

[15] A. Hölzer, M. Sommerfeld, New simple correlation formula for the drag coefficient of non-spherical particles, Powder Technology 184 (3) (2008) 361 – 365.

[16] G. A. Bokkers, M. V. S. Annaland, J. A. M. Kuipers, Mixing and segregation in a bidisperse gas-solid fluidised bed: a numerical and experimental study, Powder Technology 140 (3) (2004) 176–186.

[17] D. L. Koch, R. J. Hill, Intertial effects in suspension and porous-media flows, Annual Review of Fluid Mechanics 33 (33) (2003) 619–647.

[18] S. Ergun, Fluid flow through packed columns, Journal of Materials Science & Chemical Engineering 48 (2) (1952) 89–94.

[19] C. Y. Wen, Y. H. Yu, Mechanics of fluidization, Chem. Engng Prog. Symp. Ser 62 (1966) 100–111.

[20] R. J. Hill, D. L. Koch, A. J. C. Ladd, The first effects of fluid inertia on flows in ordered and random arrays of spheres, Journal of Fluid Mechanics 448 (2001) 213–241.

[21] R. J. Hill, D. L. Koch, A. J. C. Ladd, Moderate-Reynolds-number flows in ordered and random arrays of spheres, Journal of Fluid Mechanics 448 (2001) 243–278.

[22] M. A. V. Der Hoef, R. Beetstra, J. A. M. Kuipers, Lattice-Boltzmann simulations of low-Reynolds-number flow past mono- and bidisperse arrays of spheres : results for the permeability and drag force, Journal of Fluid Mechanics 528 (2005) 233–254.

[23] R. Beetstra, M. A. V. Der Hoef, J. A. M. Kuipers, Drag force of intermediate Reynolds number flow past mono- and bidisperse arrays of spheres, AICHE Journal 53 (2) (2007) 489–501.

[24] L. W. Rong, K. J. Dong, A. B. Yu, Lattice-Boltzmann simulation of fluid flow through packed beds of uniform spheres: Effect of porosity, Chemical Engineering Science 99 (2013) 44–58.

[25] L. W. Rong, K. J. Dong, A. B. Yu, Lattice-Boltzmann simulation of fluid flow through packed Beds of spheres: Effect of particle size distribution, Chemical Engineering Science 116 (2014) 508–523.

[26] Q. Zhou, L. Fan, Direct numerical simulation of low-Reynolds-number flow past arrays of rotating spheres, Journal of Fluid Mechanics 765 (2015) 396–423.

[27] Q. Zhou, L. Fan, Direct numerical simulation of moderate-Reynolds-number flow past arrays of rotating spheres, Physics of Fluids 27 (7) (2015) 073306.

[28] A. Hölzer, M. Sommerfeld, Lattice Boltzmann simulations to determine drag, lift and torque acting on non-spherical particles, Computers & Fluids 38 (3) (2009) 572–589.

[29] L. W. Rong, Z. Zhou, A. B. Yu, Lattice Boltzmann simulation of fluid flow through packed beds of uniform ellipsoids, Powder Technology 285 (2015) 146–156.

[30] Y. J. Guan, R. Guadarrama-Lara, X. D. Jia, K. Zhang, D. S. Wen, Lattice boltzmann simulation of flow past a non-spherical particle, Advanced Powder Technology 28 (6) (2017) 1486 – 1494.

[31] A. K. Saha, Three-dimensional numerical study of flow and heat transfer from a cube placed in a uniform flow, International Journal of Heat and Fluid Flow 27 (1) (2006) 80–94.

[32] N. Kishore, S. Gu, Momentum and heat transfer phenomena of spheroid particles at moderate Reynolds and Prandtl numbers, International Journal of Heat and Mass Transfer 54 (11) (2011) 2595–2601.

[33] A. Richter, P. A. Nikrityuk, Drag forces and heat transfer coefficients for spherical, cuboidal and ellipsoidal particles in cross flow at sub-critical Reynolds numbers, International Journal of Heat and Mass Transfer 55 (4) (2012) 1343–1354.

[34] A. Richter, P. A. Nikrityuk, New correlations for heat and fluid flow past ellipsoidal and cubic particles at different angles of attack, Powder Technology 249 (2013) 463–474.

[35] Y. Wen, M. A. Jog, Variable property, steady, axi-symmetric, laminar, continuum plasma flow over spheroidal particles, International Journal of Heat and Fluid Flow 26 (5) (2005) 780–791.

[36] C. R. Reddy, N. Kishore, Momentum and heat transfer phenomena of confined spheroid particles in power-law liquids, Industrial & Engineering Chemistry Research 53 (2) (2013) 989–998.

[37] J. Gan, Z. Zhou, A. B. Yu, Particle scale study of heat transfer in packed and fluidized beds of ellipsoidal particles, Chemical Engineering Science 144 (2016) 201–215.

[38] C. S. Peskin, Numerical analysis of blood flow in the heart, Journal of Computational Physics 25 (3) (1977) 220–252.

[39] H. Zhang, A. B. Yu, W. Q. Zhong, Y. Q. Tan, A combined TLBM-IBM-DEM scheme for simulating isothermal particulate flow in fluid, International Journal of Heat and Mass Transfer 91 (2015) 178–189.

[40] H. Zhang, H. Z. Yuan, F. X. Trias, A. B. Yu, Y. Q. Tan, A. Oliva, Particulate Immersed Boundary Method for complex fluid–particle interaction problems with heat transfer, Computers & Mathematics with Applications 71 (1) (2016) 391–407.

[41] Y. H. Qian, D. D'Humières, P. Lallemand, Lattice BGK Models for Navier-Stokes Equation, Europhysics Letters 17 (6BIS) (1992) 479.

[42] X. He, S. Chen, G. D. Doolen, A novel thermal model for the lattice Boltzmann method in incompressible limit, Journal of Computational Physics 146 (1) (1998) 282–300.

[43] X. D. Niu, C. Shu, Y. T. Chew, Y. Peng, A momentum exchange-based immersed boundary-lattice Boltzmann method for simulating incompressible viscous flows, Physics Letters A 354 (3) (2006) 173 – 182.

[44] W. Ren, C. Shu, J. Wu, W. Yang, Boundary condition-enforced immersed boundary method for thermal flow problems with Dirichlet temperature condition and its applications, Computers & Fluids 57 (2012) 40–51.

[45] X. Yue, H. Zhang, C. Ke, C. Luo, S. Shu, Y. Tan, C. Feng, A GPU-based discrete element modeling code and its application in die filling, Computers & Fluids 110 (2015) 235–244.

[46] H. Zhang, F. X. Trias, A. Oliva, D. Yang, Y. Tan, S. Shu, Y. Sheng, PIBM: Particulate immersed boundary method for fluid-particle interaction problems , Powder Technology 272 (2015) 1–13.

[47] Y. Hu, D. Li, S. Shu, X. Niu, An efficient immersed boundary-lattice Boltzmann method for the simulation of thermal flow problems, Communications in Computational Physics 20 (5) (2016) 1210–1257.

[48] A. Gilmanov, F. Sotiropoulos, E. Balaras, A general reconstruction algorithm for simulating flows with complex 3D immersed boundaries on Cartesian grids, Journal of Computational Physics 191 (2) (2003) 660–669.

[49] M. Zastawny, G. Mallouppas, F. Zhao, B. V. Wachem, Derivation of drag and lift force and torque coefficients for non-spherical particles in flows, International Journal of Multiphase Flow 39 (2012) 227–239.

[50] A. Haider, O. Levenspiel, Drag coefficient and terminal velocity of spherical and nonspherical particles, Powder Technology 58 (1) (1989) 63 – 70.

[51] J. DallaValle, Micromeritics: the technology of fine particles, Pitman Pub. Corp., 1948.

[52] H. Schlichting, K. Gersten, Boundary-Layer Theory - 8th Revised and Enlarged Edition, Springer.

[53] A. Hölzer, M. Sommerfeld, Lattice Boltzmann simulations to determine drag, lift and torque acting on non-spherical particles, Computers & Fluids 38 (3) (2009) 572–589.

[54] A. Richter, P. A. Nikrityuk, Drag forces and heat transfer coefficients for spherical, cuboidal and ellipsoidal particles in cross flow at sub-critical

Reynolds numbers, International Journal of Heat Mass Transfer 55 (4) (2012) 1343–1354.

[55] P. Bagchi, S. Balachandar, M. Y. Ha, Direct numerical simulation of flow and heat transfer from a sphere in a uniform cross-flow, Journal of Fluids Engineering 123 (2) (2001) 347–358.

[56] W. E. Ranz, Evaporation from drops, Chemical Engineering Progress 48 (1952) 141–146.

[57] E. V. Vdi, VDI Heat Atlas, Springer, Berlin, 2010.

[58] S. Whitaker, Forced convection heat transfer correlations for flow in pipes, past flat plates, single cylinders, single spheres, and for flow in packed beds and tube bundles, AICHE Journal 18 (2) (1972) 361–371.

[59] H. Yow, M. Pitt, A. Salman, Drag correlations for particles of regular shape, Advanced Powder Technology 16 (4) (2005) 363 – 372.